UNIVERSITY OF CALIFORNIA SAN DIEGO

Design principles for locomotion synchronization in undulatory robot groups

A Thesis submitted in partial satisfaction of the requirements
for the degree Master of Science

in

Engineering Sciences (Mechanical Engineering)

by

Zhuonan Hao

Committee in charge:

Professor Nicholas G. Gravish, Chair
Professor Sonia Martinez Diaz
Professor Michael T. Tolley

2021

The Thesis of Zhuonan Hao is approved, and it is acceptable in quality and form for publication on microfilm and electronically.

University of California San Diego

2021

TABLE OF CONTENTS

LIST OF FIGURES

LIST OF TABLES

ACKNOWLEDGEMENTS

First of all, I would like to sincerely appreciate my advisor Prof. Nicholas Gravish for the opportunity to work in Gravish lab. The research is inspired by his innovative cognition on swarm undualtory swimming and accomplished under the continuously guidance. Without his knowledge and support, I cannot put all my tentative ideas into practice timely and keep refining the core idea.

Besides, I want to thank all my lab members, Wei, Yudong and all the rest members who have involved in my research project and helped me overcome all kinds of challenges and difficulties. Wei led me to explore feasible application of oscillation theories on robot control with solid academic background and profound experience. Yudong shared his insights on robot design and participated majority of robot experiments with constructive suggestions.

Last but not least, I would also express my thanks to my thesis committee members, Prof. Sonia Martinez and Prof. Michael Tolley for attending my thesis defense with valuable time and precious advice.

ABSTRACT OF THE THESIS

Design principles for locomotion synchronization in undulatory robot groups

by

Zhuonan Hao

Master of Science in Engineering Sciences (Mechanical Engineering)

University of California San Diego, 2021

Professor Nicholas G. Gravish, Chair

Many group of organisms that live in proximity are capable of complicated collective movement, which occurs via periodic oscillation of the individuals. One of the fundamental goal for swarm robotics study is to understand how effective and robust the collective behaviors can emerge from simple principles of interaction. In this context, we characterize the motion behaviors of swimming animals that move through lateral body undulation with multi-link robots and demonstrate that phase adaption can be achieved through the proposed control law. Critically, the ability to achieve phase synchronization is driven through contact interactions between adjacent robots without the requirement for network communication or motion planning. Through bio-inspired experiment and simulation, we demonstrate that collective in-phase and opposite-

phase behaviors can arise passively through intermittent collision events, and furthermore we provide principles for control architecture to achieve self-organization in swarms.

Chapter 1

Introduction

Many swimming microorganisms are capable of synchronizing the body or appendage motion by interacting with their neighbors. Recent studies suggest that both long-range hydrodynamic interactions [1, 2] and short-range steric interactions [3, 4] can bring about the stable collective motions. For small organisms such as bacteria the synchronized motion of cilia [5] and flagella [6] are driven by fluid-mechanical interactions. However, in larger organisms such as the worm *C. elegans* hydrodynamic interactions are less important and instead steric hindrance become the predominant factor for gait synchronization [7]. Even for smaller systems mechanical contact interactions may be of importance in high-density population scenario [8]. Our studies propose a neuromechanical hypothesis for emergent synchronization through steric contact and we examine the group interactions in experiments with undulatory robot swarms.

C. elegans is observed to produce undulatory movements by a propagating sinusoidal wave, traveling from head to tail [9]. Recent studies have determined that intermittent mechanical contact is responsible for synchronization of the undulatory gaits of groups [7]. Biomechanical and neural experiments have demonstrated that the generation of this wave is largely through local proprioceptive reflex responses along the body that sense the local body bending and generate a bending actuation in response [10]. Thus, the propagation of the body bending wave occurs as a

"reflex chain" in which the wave propagation doesn't involve communication between oscillators and instead responds only to the bending state of the local body region. Experiments have demonstrated this local oscillator principle by isolating regions of the body and showing that a propagating wave is halted at a body region where bending is inhibited.

In the present work, we hypothesize that local reflex responses from body bending can enable synchronization of bending movement between neighboring swimmers that make contact with each other. When two undulatory swimmers make contact they will inhibit the bending motion and thus will cause a phase disruption to the swimming gait. The ability for these systems to adjust each other's phase through contact may give rise to synchronization phenomena. Critically this process would not require communication between the systems and thus could greatly simplify coordination of robot groups. In the following we will demonstrate theoretically and experimentally that local oscillators with proprioceptive feedback enable synchronization. We further demonstrate how an inhibitory versus excitatory proprioceptive gain controls whether robots synchronize to in-phase versus opposite-phase motion. We lastly demonstrate how this is useful for emergent coordination of snake-like robots to traverse narrow gaps.

Chapter 2

Modelling and Control of Undulatory Swarm System

Drawing inspiration from biology, we envision a multi-link robotic locomotor (snake-like) to simulate the undulatory swimming in *C.elegans* swarms. The simple low-DoF robot has been extensively studied and modelled in the context of wheeled, frictional, fluid, and granular locomotion at various levels of detail [11, 12, 13, 14]. The chapter mainly covers mechanical design of snake-like robot and control architectures of undulatory locomotion.

2.1 Design of snake-like robot

Undulatory locomotors can be emulated with multi-link articulated robots composed of n links connected with $n-1$ actuated joints (Figure 2.1 (a)). Though the structural analogue compromises with continuous deformation nature of many swimming animals, the simplification bypasses the control difficulty of soft matters and caters our interests on the emergence of collective behavior. Besides, the rigid entities are friendly to batch manufacture and assembly with the assistance of rapid prototyping, satisfying our needs for group robot experiments (Figure

2.1 (b)).The multi-link robot can propel itself by generating a travelling wave along its body through body-enevvioreent interaction with environment. Given that the study emphasizes on the influence of mechanical contact, forward driving force is not necessary to be produced by hydro–environment. Instead, we design scale appendages on the bottom surface to generate anisotropic friction between robot body and the ground medium (Figure 2.1 (c)). Some essential geometric values (Figure 2.1 (d)) are listed in Table 2.1. In the following works, the simple 3-link and 4-link models are adopted for demonstration.

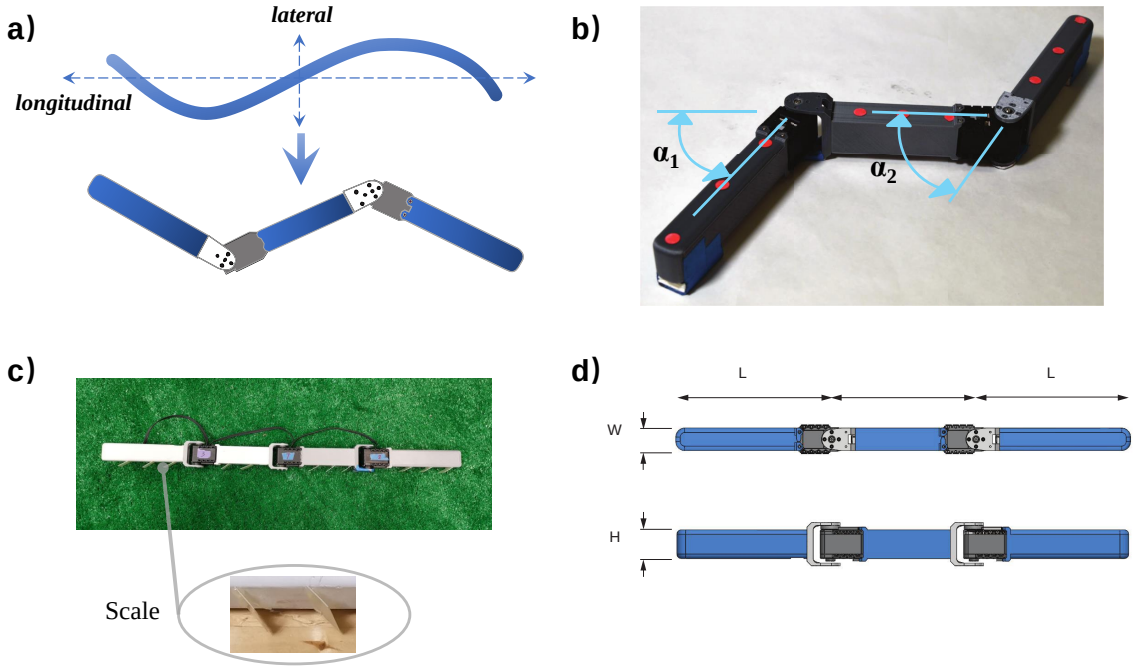

Figure 2.1: Mechanical model of undulatory robotic locomotor. (a) The continuous deformable body can be modeled as multi-link robot. (b) Three-link robot is composited of three 3D-printed body links and two actuated motors. (c) Scale appendages on bottom surface provide anisotropic friction interacting with grass ground. (d) Robot geometry parameter illustration.

Table 2.1: Robot geometry table

Parameter	Value
W	0.015 m
L	0.162 m
H	0.025 m

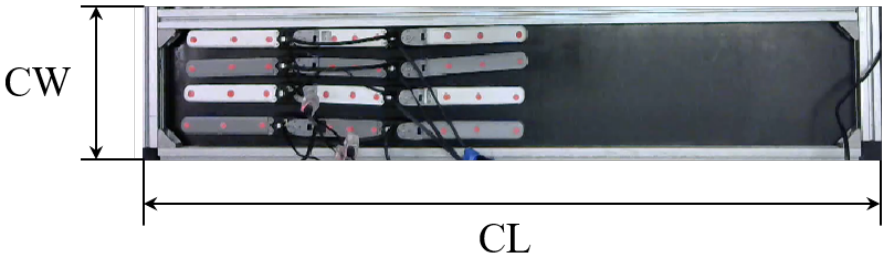

Figure 2.2: Robot group interacts inside the rectangular field.

The swarm system is designed to observe the collective behavior of two or more three-link robots interacting within a confined area. The locomotion space is created as a rectangular field with exact channel length (CL) of $1m$ and adjustable channel width (CW) varying from $0.10m$ to $0.25m$ to accommodate robot swarms (Figure 2.2).

2.2 Body oscillation control

Periodic locomotion pattern of robot comes from the actuated joint with with either position control through appropriate feedback, or commanded torque through motor's current. The joint undergoes periodic actuation signal such that $\alpha(t) = \alpha(t+T)$, where T is the time of repetition. The implementation process can be classified broadly into two types: time-dependent (open-loop) and autonomous (closed-loop):

Time-dependent	**Autonomous**
$\dot{x}(t) = f(x,t)$	$\dot{x}(t) = f(x,\dot{x})$
$f(x,t) = f(x,t+T)$	$x(t) = x(t+T)$

Time-dependent forcing is arguably the most prevalent method of joint actuation and consists of open-loop trajectories, and feedback controlled trajectory tracking. A common method of actuating many robot joints employs a simple proportional position-feedback control scheme

as:

$$f(x,t) = K(x_{ref}(t) - x). \tag{2.1}$$

In time-dependent actuation the system is "locked in" to a customized actuation phase and the control system or the open-loop dynamics will track this phase. If we ignore higher-level control methods and assume that the system is driven with an invariant reference trajectory, then gait compatibility will on be achievable through appropriate spatial rearrangement [15].

Autonomous forcing is prevalent in the areas of central pattern generators (CPGs) and limit cycle oscillator actuation schemes. In this mode of actuation the motor command signal is only dependent on the instantaneous state of the motor. For example a common limit cycle oscillator used to drive oscillatory movements in robots is:

$$f(x,\dot{x}) = -kx + (\varepsilon - cx^2)\dot{x}. \tag{2.2}$$

a generic second order Van Der Pol oscillator [16]. Systems that are driven through autonomous feedback from impulsive contact interactions can slip and drift in their actuation phase and thus have the capacity for gait compatibility by directly synchronizing their gaits [17]. The capacity for phase drift of limit cycle oscillators is a defining feature of myriad synchronization phenomena in biological and mechanical systems.

Give that many autonomous control realized through second order systems are highly associated with the body mechanics, a preliminary study on robot dynamics are essentially required before the model-based control architectures design [18]. The computation model may become significantly complicated and expensive with the increasing complexity of body structure. Besides, many systematic parameters, for example nonlinearity and damping coefficient in Van Der Por equation, are always under a fine tuning process in order to attain a reliable limit cycle behavior. Therefore, we expect to execute a model-free control scheme for robot joints combining the simplicity of position-feedback loop and self-sustained ability of autonomous

system. The knowledge of limit cycle models and CPGs networks make major contribution to the establishment of the self-organized system.

2.2.1 Limit cycle systems for motor actuation

Limit cycle system, a.k.a. oscillator system, is an autonomous dynamical system with the defining property of limit cycle attractor(s) [19]. The concept has been extensively used in robotics fields for its structural stability: (a) the systems can produce the periodic oscillations spontaneously, (b) the oscillation amplitude is robust and resistant against transient perturbation with asymptotic return trajectory, and (c) the oscillation phase is marginal stable. One can easily change the phase point along the rotation direction. Lots of studies have been accomplished to introduce oscillator models into robot control architecture [20, 21].

Interestingly, in contrast to second order oscillators, phase oscillators define straightforwardly in the phase space with concise form:

$$\dot{\phi} = \omega + p(\phi). \tag{2.3}$$

The simplified model facilitate the investigation of synchronization effect among interacting oscillators, i.e. Kuramoto oscillators [22]. By introducing radius and even frequency evolution into the dynamic, phase oscillators have a wide range of application on practical control problems. An heuristic example of robot dog *PUPPY II* fulfills an adaptive frequency walking gait through Hopf oscillator [23]. The controller takes the form of:

$$\begin{aligned} \dot{\phi} &= \omega - \frac{1}{r}\sin\phi y \\ \dot{r} &= (\mu - r^2)r + \cos\phi y \\ \dot{\omega} &= -\frac{1}{\tau}\sin\phi y \end{aligned} \tag{2.4}$$

where r, ϕ and ω represent states of amplitude, phase and frequency respectively. The sensory

input y modulates the oscillation status in response to external stimuli, and the oscillatory output:

$$u = r\cos\phi \tag{2.5}$$

is used as position point for motor. The framework elaborates how oscillator models can be exploited to generate adaptive oscillation regrading system-environment interactions.

2.2.2 Central pattern generators (CPGs) for undulatory locomotion

For multi-link robot, the communication between joints play a crucial role in the locomotion patterns. A failure on communication may result in disordered motion behaviors. CPGs network, as a decentralized control architecture, are introduced to tackle the joint-joint communication problem.

The concept of CPGs are firstly raised last century by the inspiration of some neurobiological observations: both invertebrate and vertebrate animals are capable of generating periodical activities, such as chewing and breathing, without any demands of sensory information [24]. The nature of animals motivates roboticist to extensively investigate control mechanisms of bio-inspired robots to attain better locomotor skills. The CPGs networks have been further developed with the incorporation of neuronal oscillator models to produce various locomotion patterns [25]. A paradigm of CPGs on undulatory robots presents a well-designed control architecture for generating swimming locomotion as [26]:

$$\dot{\theta}_i = 2\pi\nu_i + \sum_j w_{ij}\sin(\theta_j - \theta_i - \phi_{ij}). \tag{2.6}$$

the time evolution of i^{th} oscillator's phase θ_i, is determined by the intrinsic frequency ν_i and inter-CPG couplings concerning the weights w_{ij} and the phase biases ϕ_{ij}.

Chapter 3

Collision-driven Adaptive Phase Control Scheme

The generation of periodic shape change in snake-like robots comes from the harmonic actuation source. Chapter 2 shows that the common method to generate autonomous oscillations is to actuate as limit cycle system. Inspired by the structural simplicity of adaptive frequency oscillators in section 2.2.1, we firstly propose an adaptive phase control architecture through functional modification on Hopf oscillator. A toy model is then utilized to provide physical evidence of phase adaption and mathematical validation of convergence under proposed control framework. Besides, phase return map is introduced to evaluate the performance of the controller. Lastly, the design principles of phase adaption between collision-coupled oscillators are discussed in detail.

3.1 Amplitude-controlled phase oscillator: Hopf oscillator

Hopf oscillator defines in Phase-Radius coordinate system (PRCS) with an evolution law for both oscillatory phase ϕ and amplitude r in the following way:

$$\begin{aligned} \dot{\phi} &= \omega (= const), \\ \dot{r} &= (\mu - r^2) r. \end{aligned} \tag{3.1}$$

where parameter ω and μ govern the intrinsic frequency and steady oscillatory amplitude, respectively. With appropriate transformation, the system can be equivalently converted to Cartesian coordinate system (QCS):

$$\begin{aligned} \dot{x} &= (\mu - x^2 - y^2) x - \omega y, \\ \dot{y} &= (\mu - x^2 - y^2) y + \omega x. \end{aligned} \tag{3.2}$$

The system possesses the following properties: (a) frequency is invariant, (b) amplitude asymptotically converges to $\sqrt{\mu}$, and (c) oscillatory output signals $x = r\cos\phi$ and $y = r\sin\phi$ are harmonic, which can be used for motor actuation.

3.2 Collision-driven adaptive phase Hopf oscillator

In Equation 3.1, oscillator phase ϕ grows uniformly in time with evolution rate ω. However, phase is not necessarily proportional with time under our control architecture. Here, we propose a generic perturbation term p_ϕ acting on the phase to decouple the relationship with time:

$$\begin{aligned} \dot{\phi} &= \omega + p_\phi, \\ \dot{r} &= (\mu - r^2) r. \end{aligned} \tag{3.3}$$

furthermore, we found the perturbation p_ϕ can be expressed with:

$$p_\phi = \gamma\, g(\phi_e, \phi). \tag{3.4}$$

where function $g(\phi_e, \phi)$ allows the oscillator to proactively receive the physical collision information from the external environment and adjust internal phase ϕ with the knowledge of estimated phase ϕ_e, and gain γ scales the adaption effect. Here we declare $g(\phi_e, \phi)$ as adaptive function and γ as proprioceptive gain respectively. They are all of central importance on collective motion patterns.

The system output

$$x = r\, \cos\phi. \tag{3.5}$$

is likewise used as position point for motor. We realize that the derivation of x, i.e. $\dot{x}$, represents velocity information in a physical sense. For most of servo motors, both position and velocity are measurable states. Besides, through Equation 3.2, state y and $\dot{y}$ are also accessible as long as x and $\dot{x}$ are provided. Two feasible approaches are demonstrated in Figure 3.1.

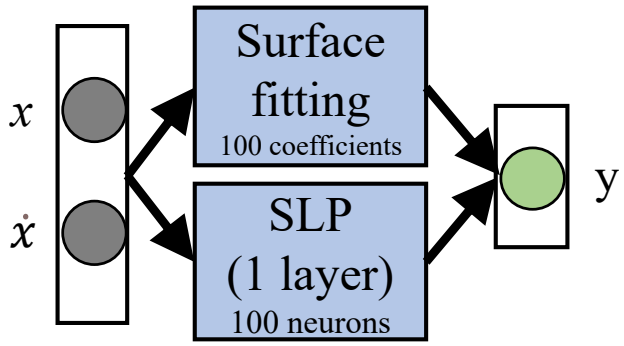

Figure 3.1: Two approaches to Estimate state y with states x and $\dot{x}$: (a) surface fitting, (b) single layer perceptron (SLP).

Therefore, the challenging problem is to design an appropriate input signal ϕ_e as the estimated phase to perturb phase dynamic with internal phase ϕ. The detail will be intuitively

explained by a physical toy model.

3.2.1 Toy model: contact coupled blocks

Recall our purpose is to adapt agent phase between two or more snake-like robots, the interaction process can be simplified with contact coupled blocks, envisioning each of them represents one of snake-like robot and is actuated with proposed adaptive phase controller (Figure 3.2 (a)).

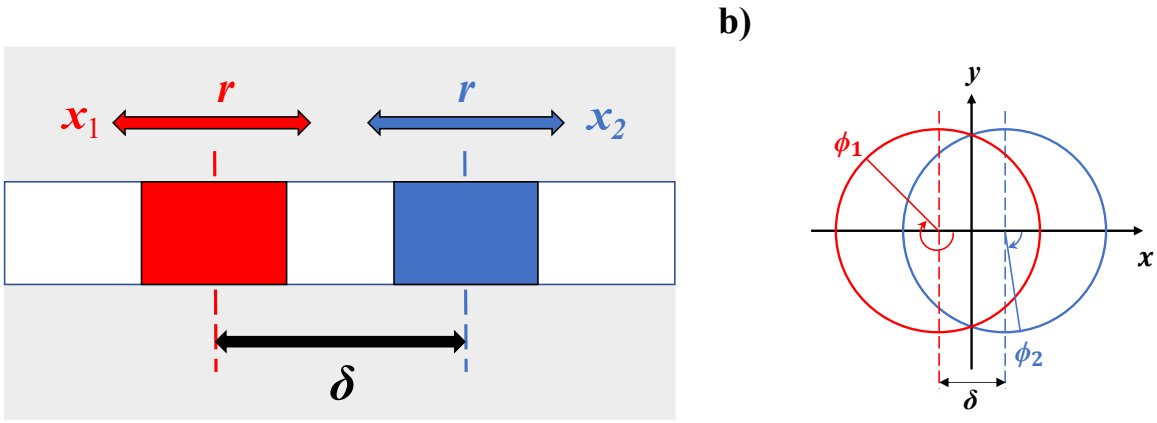

Figure 3.2: The motion of blocks can be equivalently describe by limit cycle diagram. (a) Contact coupled blocks. (b) Limit cycle diagram.

Assume each block (blue and red) is actuated by Hopf oscillator (Equation 3.1) and performs harmonic motion around respective equilibrium position by taking position $x = r\cos\phi$. They are initially separated by a specific distance δ and strike each other when position overlapping. The motion behavior can be equivalently described in the limit cycle diagram, where two phase points move along clockwise direction (Figure 3.2 (b)). We construct the phase dynamic with perturbation as:

$$\begin{aligned} \dot{\phi}_1 &= \omega + \gamma\, g(\phi_{e_1}, \phi_1), \\ \dot{\phi}_2 &= \omega + \gamma\, g(\phi_{e_2}, \phi_2). \end{aligned} \tag{3.6}$$

We expect the estimated state ϕ_{e_i} can sense the external collision events, and then act as

the feedback to adjust internal phase ϕ simultaneously. Besides, the adjustment effect should be deactivated for no collision scenarios so that it works "in step" with outside process only.

Given that collision causes the sudden change in motion behavior of two or more bodies due to exerting forces, the motion variables, e.g. position, velocity and acceleration, are exploitable for the kinematics analysis. Besides, the actuated motor always provides the better accuracy for the position and velocity measurement, therefore we attentively propose the mapping $\mathbb{F}$ to estimate phase ϕ_{e_i} with measured position x and velocity $\dot{x}$:

$$\mathbb{F} : (x, \dot{x}) \rightarrow \phi_e \tag{3.7}$$

Recall the relationship between Phase-Radius coordinate system (PRCS) and Cartesian coordinate system (QCS) can be always converted by an appropriate transformation $\mathbb{T}$:

$$[\phi, r]^T = \mathbb{T}(x, y). \tag{3.8}$$

A common used trick is realized by polar coordinate transformation $\mathbb{T}_p$:

$$\begin{aligned} \mathbb{T}_{p_\phi} &: \phi = \tan^{-1}(\frac{y}{x}) \mod 2\pi, \\ \mathbb{T}_{p_r} &: r = \sqrt{x^2 + y^2}. \end{aligned} \tag{3.9}$$

Considering the nonlinearity of Equation 3.2, phase oscillators do not admit second-order relation $\dot{x} = y$, or a physical "position-velocity" relationship. However, as mentioned, x and $\dot{x}$ can be used to estimate state y as mapping $\mathbb{G}$, i.e.,

$$\dot{x} = (\mu - x^2 - y^2)x - \omega y \Leftrightarrow y = \mathbb{G}(x, \dot{x}). \tag{3.10}$$

Therefore, mapping $\mathbb{F}$ can be realized through the combination operation of mapping $\mathbb{G}$

and $\mathbb{T}_{p_\phi}$, i.e.,

$$\phi_e = \mathbb{F}(x,\dot{x}) = \mathbb{T}_{p_\phi}(x,y) = \mathbb{T}_{p_\phi}(x,\mathbb{G}(x,\dot{x})). \tag{3.11}$$

3.2.2 Collision assumptions

Typically, collision in the context can be divided into two types, 1) "head-on" collision (Figure 3.3 (a)): two objects collide with different velocity direction, and 2) "rear-end" collision (Figure 3.3 (b)): two objects collide with the same velocity direction but different velocity magnitude (the rear move faster than the front).

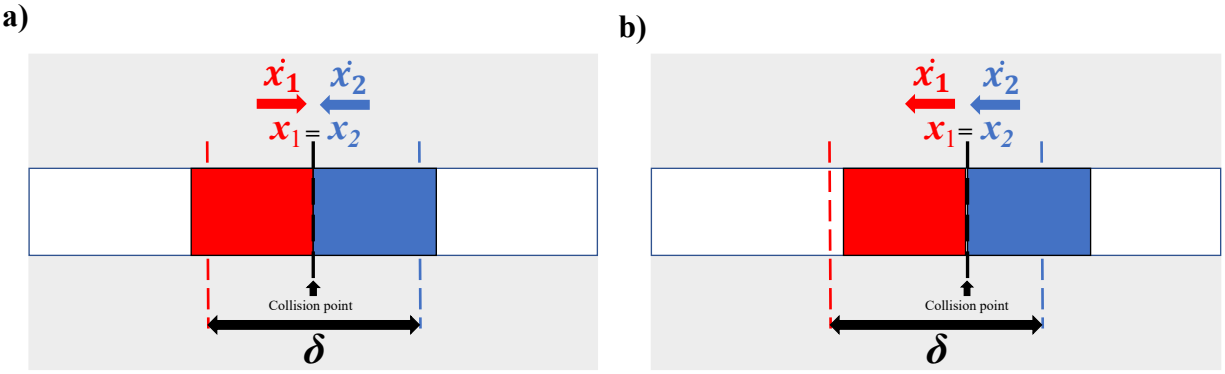

Figure 3.3: Two types of collision model. (a) Head-on collision. (b) Rear-end collision.

According to the definition of collisions, the **contact condition** can be described with physical symbols as below:

	Head-on collision	**Rear-end collision**
	$x_1 = x_2$	$x_1 = x_2$
	$\dot{x}_1\dot{x}_2 < 0$	$\dot{x}_2 \leq \dot{x}_1 < 0$ or $\dot{x}_1 > \dot{x}_2 \geq 0$

We assume each position controlled joint is with enough stiffness such that when head-on collision happens, two objects stop moving immediately until separation, i.e. velocity drops to 0, and when rear-end collision happens, the high speed object tether the low speed object and move

together with the low speed object until separation. Therefore, the **in-contact condition** can be described as:

Head-on collision	**Rear-end collision**
$x_i^* = x_i^-$	$x_h^* = x_l^*$
$\dot{x_i^*} = 0$	$\dot{x_h^*} = \dot{x_l^*}$

Note: superscript '*' and '-' represent during and before collision state, subscript 'h' and 'l' represent high speed and low speed object.

By the study of mapping $\mathbb{G} : (x, \dot{x}) \rightarrow y$ (Figure 3.4), we find state y is close to 0 when velocity state $\dot{x} \equiv 0$.

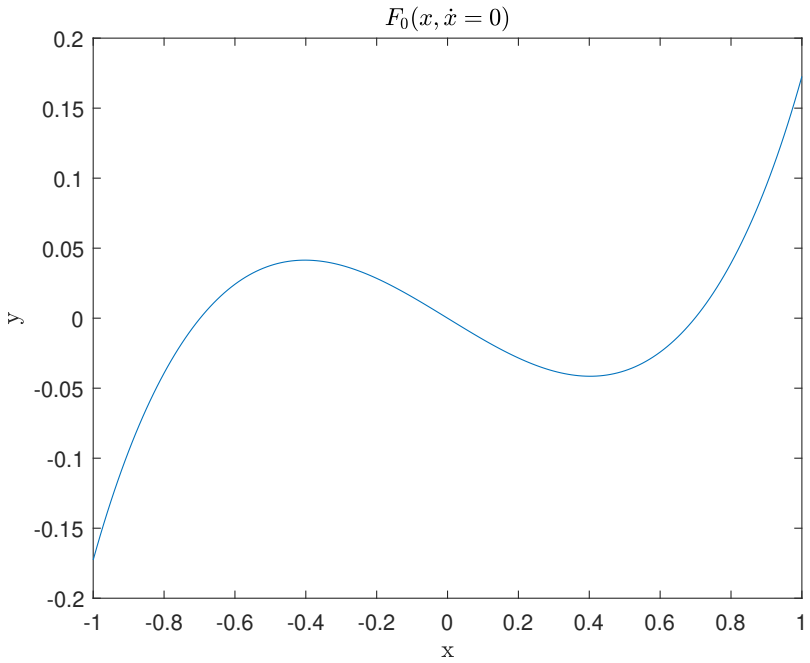

Figure 3.4: $\mathbb{G} : (x, \dot{x}) \rightarrow y$.

Therefore, through Equation 3.9, the estimated phase ϕ_e become around either 0 or pi in collision process. However, canonical phase dynamic $\dot{\phi} = \omega$, cannot immediately change phase ϕ to 0 or pi. That allows us to attentively construct the adaptive function by the difference between

estimated phase and internal phase. We can employ a *sin* function to normalize this difference:

$$\begin{aligned}\dot{\phi}_1 &= \omega + \gamma \sin(\phi_{e1} - \phi_1),\\ \dot{\phi}_2 &= \omega + \gamma \sin(\phi_{e2} - \phi_2).\end{aligned} \tag{3.12}$$

Noticeably, the adaptive function is void when no collision because estimated phase ϕ_e almost equal to internal phase ϕ. Only when estimated phase ϕ_e have a sudden change caused by collision, the adaptive function is activated.

3.2.3 Collision Dynamic Analysis

Collision dynamic analysis is useful for phase convergence study with the assistance of limit cycle diagram. Because the rear-end collision only have little influence on phase disruption, the interactions driven by head-on collision will be discussed in this section. Considering the interaction between two contact coupled Hopf oscillators controlled by dynamics Equation 3.12, we introduce an intermediate variable

$$\phi_d = \phi_1 - \phi_2. \tag{3.13}$$

to represent phase difference between two oscillators. The derivative of ϕ_d is also an accessible variable with:

$$\begin{aligned}\dot{\phi}_d &= \dot{\phi}_1 - \dot{\phi}_2\\ &= \sin(\phi_{e1} - \phi_1) - \sin(\phi_{e2} - \phi_2).\end{aligned} \tag{3.14}$$

The collision process can be equivalently reflected onto limit cycle diagram. According to the relative position of collision points, i.e., the position relationship between collision position (black dashed line) and equilibrium position (red and blue dashed lines), we divide the head-on

collision into below four different scenarios.

Scenario 1: collision position is on the left of all equilibrium positions, cf., Figure 3.5.

Collision position	Contact condition	Separation condition
$x < -\frac{\delta}{2}$	$r\cos(\pi-\phi_2^-) - r\cos(\phi_1^- - \pi) = \delta$	(a) $\phi_2^+ = 2\pi - \phi_2^-$
	$\Leftrightarrow r\cos\phi_1^- - r\cos\phi_2^- = \delta$	(b) $\sin\phi_1^+ < \sin\phi_2^+$

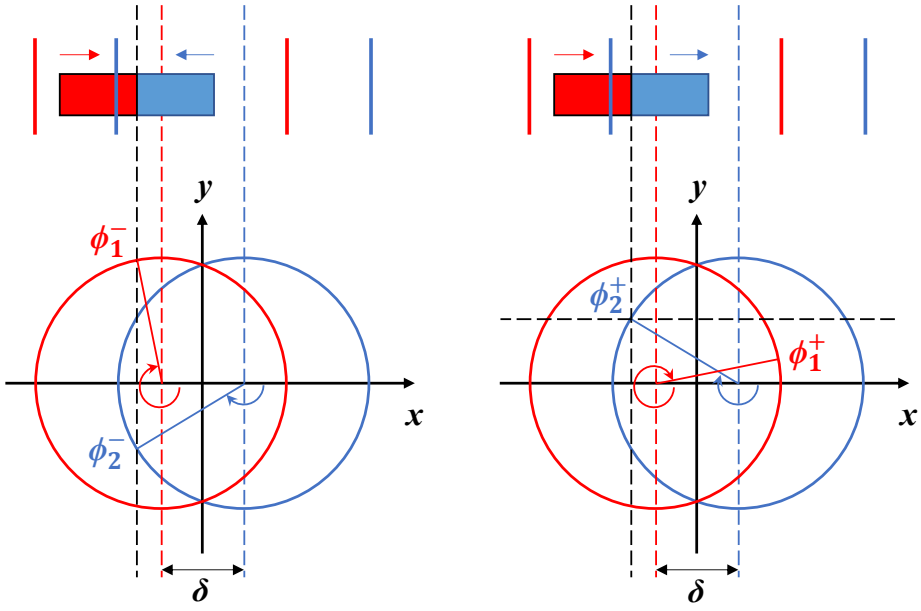

Figure 3.5: Collision position is on the left of all equilibrium positions. The contact condition (left) and separation condition (right).

Assume phase ϕ_1 is advanced to ϕ_2 before collision, i.e.,

$$\phi_d^- = \phi_1^- - \phi_2^- > 0, \tag{3.15}$$

collision assumptions in section 3.2.2 lead to:

$$\phi_{e1} = \phi_{e2} = \pi. \tag{3.16}$$

Then, Equation 3.12 and 3.14 can be rewritten as:

$$\begin{aligned}\dot{\phi}_1 &= \omega + \gamma \sin\phi_1, \\ \dot{\phi}_2 &= \omega + \gamma \sin\phi_2, \\ \dot{\phi}_d &= \gamma(\sin\phi_1 - \sin\phi_2).\end{aligned} \tag{3.17}$$

Integrate ϕ_1 and ϕ_2 over collision period $[t^-, t^+]$,

$$\int_{\phi_1^-}^{\phi_1^+} \frac{1}{\omega + \gamma \sin\phi_1} d\phi_1 = \int_{\phi_2^-}^{\phi_2^+} \frac{1}{\omega + \gamma \sin\phi_2} d\phi_2, \tag{3.18}$$

i.e.

$$\tan^{-1}\left(\frac{\omega \tan\frac{\phi_1^+}{2} + \gamma}{\sqrt{\omega^2 - \gamma^2}}\right) - \tan^{-1}\left(\frac{\omega \tan\frac{\phi_1^-}{2} + \gamma}{\sqrt{\omega^2 - \gamma^2}}\right) = \tan^{-1}\left(\frac{\omega \tan\frac{\phi_2^+}{2} + \gamma}{\sqrt{\omega^2 - \gamma^2}}\right) - \tan^{-1}\left(\frac{\omega \tan\frac{\phi_2^-}{2} + \gamma}{\sqrt{\omega^2 - \gamma^2}}\right). \tag{3.19}$$

Apply contact and separation conditions,

$$\begin{aligned}\phi_2^- &\in [\cos^{-1}(-\frac{\delta}{r}), \pi], \\ \phi_2^+ &= 2\pi - \phi_2^-, \\ \phi_1^- &= \cos^{-1}(\frac{\delta}{r} + \cos\phi_2^-) \in [\pi, \frac{3\pi}{2}] \\ &= 2\pi - \arccos(\frac{\delta}{r} + \cos\phi_2^-).\end{aligned} \tag{3.20}$$

then we have,

$$\phi_1^+ = f(\phi_2^-, \phi_2^+, \phi_1^-) = 2\tan^{-1}\left(\frac{\tan\zeta_1 \sqrt{\omega^2 - \gamma^2} - \gamma}{\omega}\right), \tag{3.21}$$

where,

$$\zeta_1 = \tan^{-1}\left(\frac{\omega \tan\frac{\phi_2^+}{2} + \gamma}{\sqrt{\omega^2 - \gamma^2}}\right) - \tan^{-1}\left(\frac{\omega \tan\frac{\phi_2^-}{2} + \gamma}{\sqrt{\omega^2 - \gamma^2}}\right) + \tan^{-1}\left(\frac{\omega \tan\frac{\phi_1^-}{2} + \gamma}{\sqrt{\omega^2 - \gamma^2}}\right).$$

Scenario 2: collision position is on the right of all equilibrium positions, cf., Figure 3.6.

Collision position	**Contact condition**	**Separation condition**
$x > \frac{\delta}{2}$	$r\cos(2\pi - \phi_1^-) - r\cos\phi_2^+ = \delta$	(a) $\phi_1^+ = 2\pi - \phi_1^-$
	$\Leftrightarrow r\cos\phi_1^- - r\cos\phi_2^- = \delta$	(b) $\sin\phi_1^+ < \sin\phi_2^+$

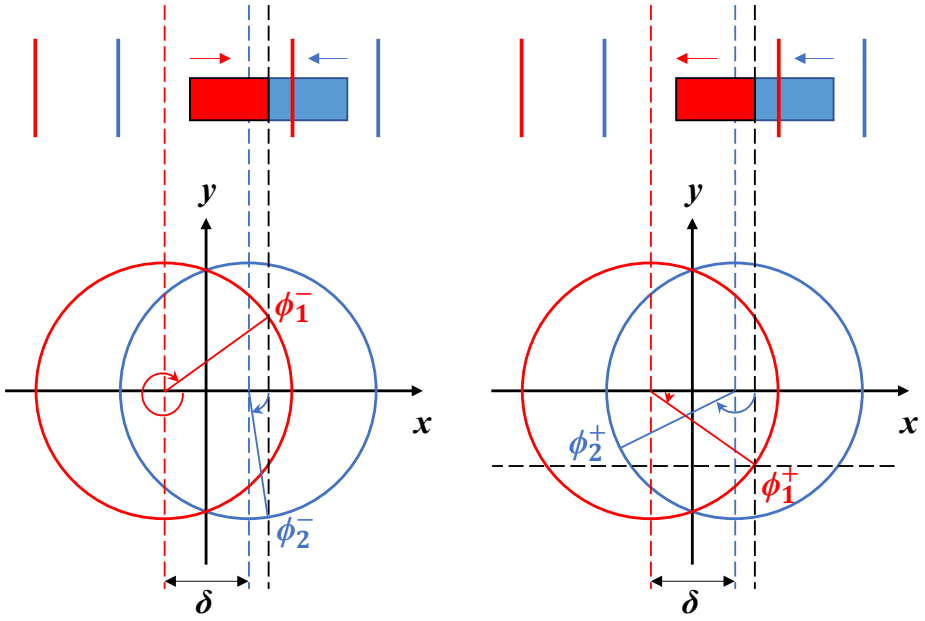

Figure 3.6: Collision position is on the right of all equilibrium positions. The contact condition (left) and separation condition (right).

Assume phase ϕ_2 is advanced to $\phi_1 - 2\pi$ before contact, i.e.

$$\phi_d^- = \phi_1^- - \phi_2^- - 2\pi < 0, \tag{3.22}$$

collision assumptions in section 3.2.2 lead to:

$$\phi_{e1} = \phi_{e2} = 0. \tag{3.23}$$

Then, Equation 3.12 and 3.14 can be rewritten as:

$$\begin{aligned} \dot{\phi}_1 &= \omega - \gamma \sin\phi_1, \\ \dot{\phi}_2 &= \omega - \gamma \sin\phi_2, \\ \dot{\phi}_d &= \gamma (\sin\phi_2 - \sin\phi_1). \end{aligned} \tag{3.24}$$

Integrate ϕ_1 and ϕ_2 over collision period $[t^-, t^+]$,

$$\int_{\phi_1^-}^{\phi_1^+} \frac{1}{\omega - \gamma \sin\phi_1} d\phi_1 = \int_{\phi_2^-}^{\phi_2^+} \frac{1}{\omega - \gamma \sin\phi_2} d\phi_2, \tag{3.25}$$

i.e.

$$\tan^{-1}(\frac{-\omega\tan\frac{\phi_1^+}{2} + \gamma}{\sqrt{\omega^2 - \gamma^2}}) - \tan^{-1}(\frac{-\omega\tan\frac{\phi_1^-}{2} + \gamma}{\sqrt{\omega^2 - \gamma^2}}) = \tan^{-1}(\frac{-\omega\tan\frac{\phi_2^+}{2} + \gamma}{\sqrt{\omega^2 - \gamma^2}}) - \tan^{-1}(\frac{-\omega\tan\frac{\phi_2^-}{2} + \gamma}{\sqrt{\omega^2 - \gamma^2}}). \tag{3.26}$$

Apply contact and separation conditions,

$$\begin{aligned} \phi_1^- &\in [2\pi - \cos^{-1}(\frac{\delta}{r}), 2\pi], \\ \phi_1^+ &= 2\pi - \phi_1^-, \\ \phi_2^- &= \cos^{-1}(\cos\phi_1^- - \frac{\delta}{r}) \in [0, \frac{\pi}{2}], \end{aligned} \tag{3.27}$$

then we have,

$$\phi_2^+ = f(\phi_1^-, \phi_1^+, \phi_2^-) = 2\tan^{-1}(\frac{\tan\zeta_2\sqrt{\omega^2 - \gamma^2} - \gamma}{-\omega}), \tag{3.28}$$

where,

$$\zeta_2 = \tan^{-1}\left(\frac{-\omega\tan\frac{\phi_1^+}{2}+\gamma}{\sqrt{\omega^2-\gamma^2}}\right) - \tan^{-1}\left(\frac{-\omega\tan\frac{\phi_1^-}{2}+\gamma}{\sqrt{\omega^2-\gamma^2}}\right) + \tan^{-1}\left(\frac{-\omega\tan\frac{\phi_2^-}{2}+\gamma}{\sqrt{\omega^2-\gamma^2}}\right).$$

Scenario 3: collision position is on the middle of left equilibrium position and origin position, cf., Figure 3.7.

Collision position	Contact condition	Separation condition
$-\frac{\delta}{2} \le x < 0$	$r\cos(2\pi-\phi_1^-)+r\cos(\pi-\phi_2^+)=\delta$	(a) $\phi_2^+ = 2\pi-\phi_2^-$
	$\Leftrightarrow r\cos\phi_1^- - r\cos\phi_2^- = \delta$	(b) $\sin\phi_2^+ \times \sin\phi_1^+ < 0$

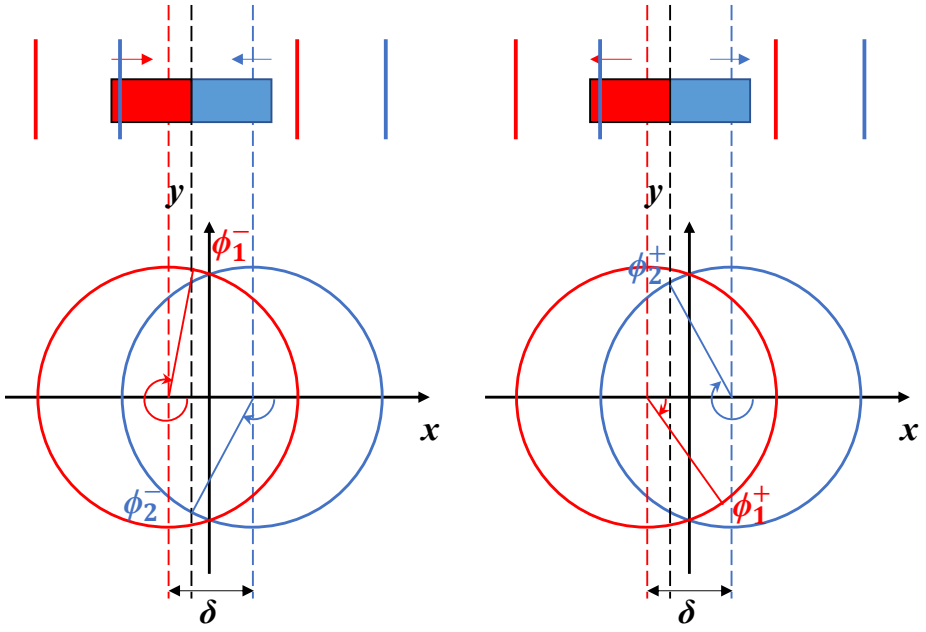

Figure 3.7: Collision position is on the middle of left equilibrium position and origin position. The contact condition (left) and separation condition (right).

Collision assumptions in section 3.2.2 lead to:

$$\phi_{e1} = 0, \phi_{e2} = \pi. \tag{3.29}$$

Then, Equation 3.12 and 3.14 can be rewritten as:

$$\begin{aligned}\dot{\phi}_1 &= \omega - \gamma \sin\phi_1, \\ \dot{\phi}_2 &= \omega + \gamma \sin\phi_2, \\ \dot{\phi}_d &= -\gamma(\sin\phi_1 + \sin\phi_2).\end{aligned} \tag{3.30}$$

Integrate ϕ_1 and ϕ_2 over collision period $[t^-, t^+]$,

$$\int_{\phi_1^-}^{\phi_1^+} \frac{1}{\omega - \sin\phi_1}\, d\phi_1 = \int_{\phi_2^-}^{\phi_2^+} \frac{1}{\omega + \sin\phi_2}\, d\phi_2, \tag{3.31}$$

i.e.

$$\tan^{-1}\left(\frac{-\omega\tan\frac{\phi_1^+}{2} + \gamma}{\sqrt{\omega^2-\gamma^2}}\right) - \tan^{-1}\left(\frac{-\omega\tan\frac{\phi_1^-}{2} + \gamma}{\sqrt{\omega^2-\gamma^2}}\right) = \tan^{-1}\left(\frac{\omega\tan\frac{\phi_2^+}{2} + \gamma}{\sqrt{\omega^2-\gamma^2}}\right) - \tan^{-1}\left(\frac{\omega\tan\frac{\phi_2^-}{2} + \gamma}{\sqrt{\omega^2-\gamma^2}}\right). \tag{3.32}$$

Apply contact and separation conditions,

$$\begin{aligned}&\phi_2^- \in [\frac{\pi}{2}, \cos^{-1}(-\frac{\delta}{r})], \\ &\phi_2^+ = 2\pi - \phi_1^-, \\ &\phi_1^- = \cos^{-1}(\cos\phi_2^- + \frac{\delta}{r}) \in [\frac{3\pi}{2}, 2\pi],\end{aligned} \tag{3.33}$$

then we have,

$$\phi_1^+ = f(\phi_2^-, \phi_2^+, \phi_1^-) = 2\tan^{-1}\left(\frac{\tan(\zeta_1')\sqrt{\omega^2-\gamma^2} - \gamma}{-\omega}\right), \tag{3.34}$$

where,

$$\zeta_1' = \tan^{-1}\left(\frac{\omega\tan\frac{\phi_1^+}{2} + 1}{\sqrt{\omega^2-1}}\right) - \tan^{-1}\left(\frac{\omega\tan\frac{\phi_1^-}{2} + 1}{\sqrt{\omega^2-1}}\right) + \tan^{-1}\left(\frac{-\omega\tan\frac{\phi_2^-}{2} + 1}{\sqrt{\omega^2-1}}\right).$$

Scenario 4: collision position is on the middle of right equilibrium position and origin position, cf., Figure 3.8.

Collision position	Contact condition	Separation condition
$0 \le x \le \frac{\delta}{2}$	$r\cos(2\pi-\phi_1^-)+r\cos(\pi-\phi_2^+)=\delta$	(a) $\phi_1^+ = 2\pi-\phi_1^-$
	$\Leftrightarrow r\cos\phi_1^- - r\cos\phi_2^- = \delta$	(b) $\sin(\phi_1^+)\times\sin(\phi_2^+)<0$

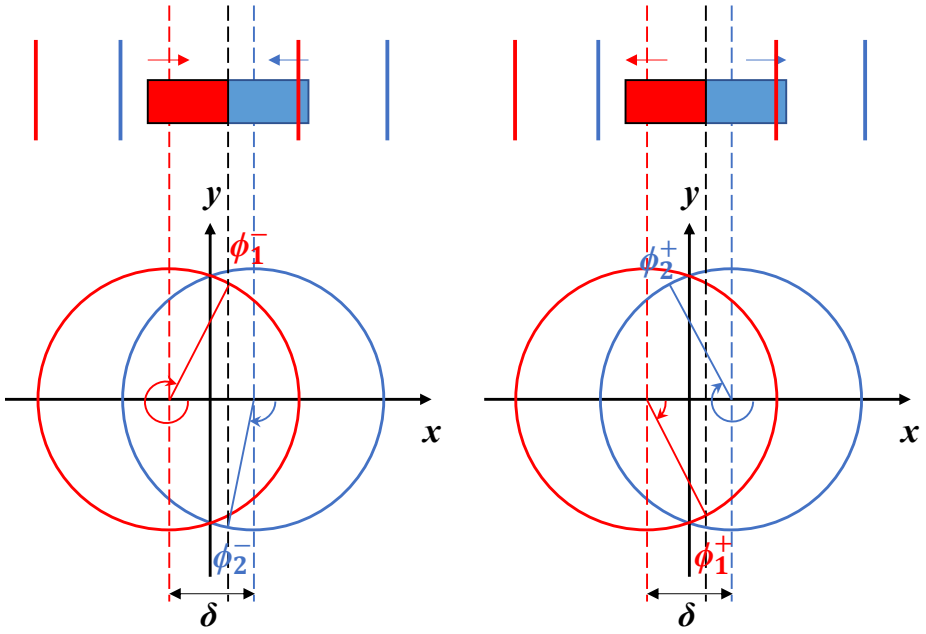

Figure 3.8: Collision position is on the middle of left equilibrium position and origin position. The contact condition (left) and separation condition (right).

Collision assumptions in section 3.2.2 lead to:

$$\phi_{e1} = 0, \phi_{e2} = \pi. \tag{3.35}$$

Then, Equation 3.12 and 3.14 can be rewritten as:

$$\begin{aligned}\dot{\phi}_1 &= \omega - \sin\phi_1,\\ \dot{\phi}_2 &= \omega + \sin\phi_2,\\ \dot{\phi}_d &= -\gamma\,(\sin\phi_1 + \sin\phi_2).\end{aligned} \tag{3.36}$$

Integrate ϕ_1 and ϕ_2 over collision period $[t^-, t^+]$,

$$\int_{\phi_1^-}^{\phi_1^+} \frac{1}{\omega - \sin\phi_1}\, d\phi_1 = \int_{\phi_2^-}^{\phi_2^+} \frac{1}{\omega + \sin\phi_2}\, d\phi_2, \tag{3.37}$$

i.e.

$$\tan^{-1}\left(\frac{-\omega\tan\frac{\phi_1^+}{2} + \gamma}{\sqrt{\omega^2-\gamma^2}}\right) - \tan^{-1}\left(\frac{-\omega\tan\frac{\phi_1^-}{2} + \gamma}{\sqrt{\omega^2-\gamma^2}}\right) = \tan^{-1}\left(\frac{\omega\tan\frac{\phi_2^+}{2} + \gamma}{\sqrt{\omega^2-\gamma^2}}\right) - \tan^{-1}\left(\frac{\omega\tan\frac{\phi_2^-}{2} + \gamma}{\sqrt{\omega^2-\gamma^2}}\right). \tag{3.38}$$

Apply contact and separation conditions,

$$\begin{aligned}&\phi_1^- \in \left[\frac{3\pi}{2}, 2\pi - \cos^{-1}\left(\frac{\delta}{r}\right)\right],\\ &\phi_1^+ = 2\pi - \phi_1^-,\\ &\phi_2^- = \cos^{-1}\left(\cos\phi_1^- - \frac{\delta}{r}\right) \in \left[\frac{\pi}{2}, \pi\right],\end{aligned} \tag{3.39}$$

then we have:

$$\phi_2^+ = f(\phi_1^-, \phi_1^+, \phi_2^-) = 2\tan^{-1}\left(\frac{\tan\zeta_2'\sqrt{\omega^2-\gamma^2} - \gamma}{\omega}\right), \tag{3.40}$$

where,

$$\zeta_2' = \tan^{-1}\left(\frac{-\omega\tan\frac{\phi_1^+}{2}+\gamma}{\sqrt{\omega^2-\gamma^2}}\right) - \tan^{-1}\left(\frac{-\omega\tan\frac{\phi_1^-}{2}+\gamma}{\sqrt{\omega^2-\gamma^2}}\right) + \tan^{-1}\left(\frac{\omega\tan\frac{\phi_2^-}{2}+\gamma}{\sqrt{\omega^2-\gamma^2}}\right).$$

3.2.4 Phase return map

The above analysis takes into account the change of individual oscillator phase from collision to collision, which motivates us to study overall phase difference change between the two collision-coupled oscillators. Phase return map is introduced here to examine the asymptotic behavior of $\Delta\phi$. With the closed form expression of both before and after collision phase, the phase difference changes from the end of the n^{th} contact to the $n+1^{th}$ contact can be characterized with mapping $\mathbb{R}$:

$$\mathbb{R} : \Delta\phi^n = \phi_1^n - \phi_2^n \rightarrow \Delta\phi^{n+1} = \phi_1^{n+1} - \phi_2^{n+1} \tag{3.41}$$

The phase return map can be generated through the numerical integration as demonstrated in section 3.2.3. One can easily address the evolution of $\Delta\phi$ along the return map with the reference line $\Delta\phi_{n+1} = \Delta\phi_n$. For example (Figure 3.9), the contact coupled blocks may start with initial phase difference $\Delta\phi_0$ of 2.5, the first-time collision leads the after-collision phase difference $\Delta\phi_1 = 2$. Because the nature of intermittent contact, the phase difference $\Delta\phi$ can maintain the same before the second-time collision. With the assistant line of $\Delta\phi_{n+1} = \Delta\phi_n$, the second-time collision starts with $\Delta\phi_1 = 2$ and ends with $\Delta\phi_2 = 1$. Keep doing so, we finally find $\Delta\phi$ asymptotically converge to 0, which indicates the in-phase synchronization is guaranteed.

Noticeably, the perpendicular distance from the curve points to line $\Delta\phi_{n+1} = \Delta\phi_n$ represent the convergence speed. From this perspective, $\Delta\phi$ has trivial convergence tendency for the large phase difference region, especially 0 and π, as a result of periodicity of *sin* function. The system therefore contain a stable anti-phase region.

Besides, the shape of phase return map is sensitive to initial separation distance δ, proprioceptive gain γ, and even the form of adaptive function $g(\circ,\circ)$, which provides us an insight into design principle for phase adaption.

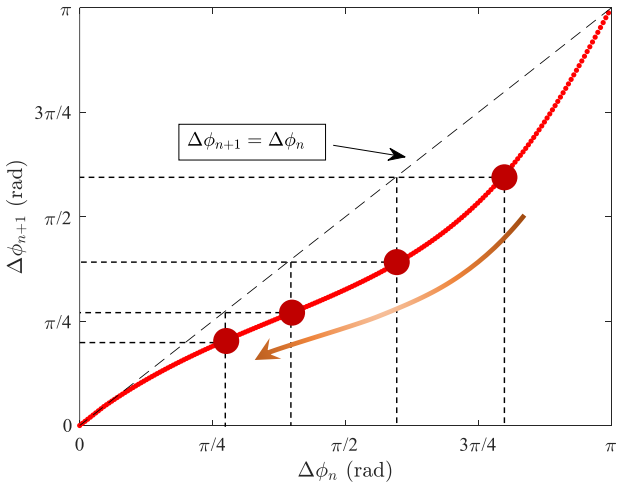

Figure 3.9: Phase return map reveals the asymptotic behavior of phase difference. Plot with numerical integration for parameter $\delta = 0, \omega = \pi, \gamma = 0.4\omega$.

3.3 Design principles

Section 3.2 presents a successful design structure for phase adaption of contact coupled oscillators. By the means of phase return map, synchronization process is also reflected on attracted curve. In this section, we discuss some design-level factors that contribute substantially to the shape of phase return map.

3.3.1 Adaptive function

Recall the adaptive function, $g(\phi_e, \phi)$, measures the difference between estimated phase and kinematic phase in Equation 3.4, a trigonometric function $\sin(\phi_e - \phi)$ has been implied in section 3.2 to regulate the kinematic phase in actual system. The periodicity and boundedness of

the function guarantee a smooth phase evolution. However, the periodicity nature results in an obvious defect: the system has the same regulation effect for both large (close to π) and small (close to 0) phase difference region. In other words, the curve of phase return map is concave. The convexity can be changed by taking alternative function form, e.g., linear function or exponential function (Figure 3.10). But in practice, these functions may break down the motors due to the loss of boundedness unless fine tune an appropriate proprioceptive gain.

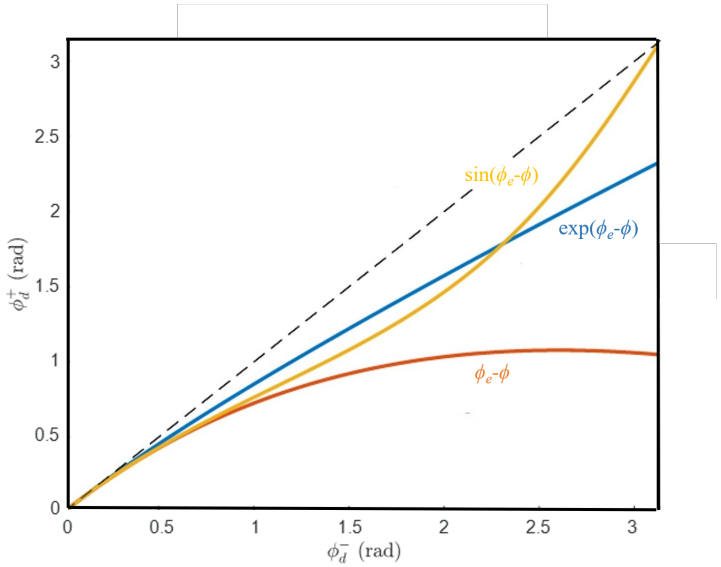

Figure 3.10: The convexity of curve changes with the adaptive function.

3.3.2 Proprioceptive gain

The feedback adaptive function, $g(\phi_e, \phi)$, is multiplied by a single proprioceptive gain term γ. In section 3.2, positive gain allows in phase behavior to emerge within finite collision events. In fact, two oscillators that make contact will synchronize to in-phase or anti-phase status dependent on the sign and magnitude of γ. Figure 3.11 illustrates results from numerical integration of collision dynamics using Equation 3.6. When $0 < \gamma < \omega$ we observe that oscillator phases always achieve synchronization. The magnitude of γ controls speed of the synchronization process. However, if γ exceeds ω the synchronization dynamics break down because the oscillatory motion

is no longer smooth. When $\gamma < 0$ the oscillator is driven to anti-phase synchronization and a $\gamma = 0$ puts the control into a purely feedforward form with no feedback and the dynamics equations can be integrated to resolve the time-dependent actuation.

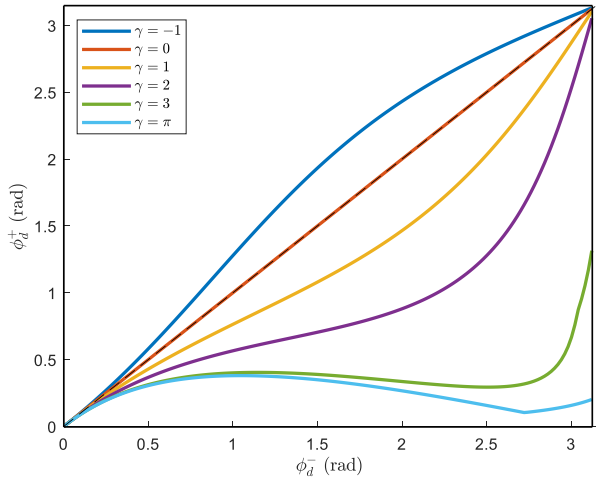

Figure 3.11: The curvature of curve depends on the proprioceeptive gain.

3.3.3 Equilibrium separation distance

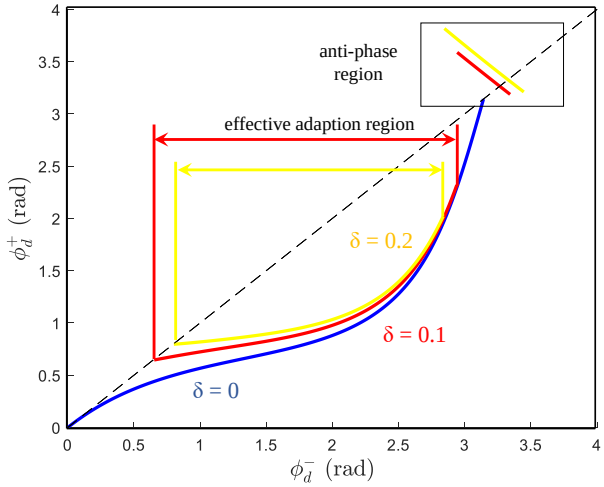

Figure 3.12: Spatial layout determine the anti-phase region and effective adaption region.

Equilibrium separation distance, δ, is used to determine contact and separation condition

in section 3.2., which play a crucial role for phase compatibility. δ have an influence on both anti-phase region and effective adaption region (Fiure 3.12). However, it is not controllable in practical control scheme. Therefore, we demonstrate the effect in section 4.3 with several exact spatial layouts.

3.4 Summary

Based on the oscillator theories, the chapter develops the collision-driven adaptive phase controller on a toy model. The analysis of collision dynamic works out the closed-form expression of individual phases. By means of phase return map, we visualize the synchronization process and study the effect of some crucial system parameters. However, all the work so far is subjected to the single joint control instead of entire robot body. In next chapter, we increase the control complexity by looking into the practical application on multi-link robot and study how these factors make a difference on collective behavior.

Chapter 4

Experimental and Simulation Demonstrations

Chapter 3 proposes a collision-drive adaptive phase algorithm in regard of single robot joint. In actual swarm system, the individual robot is composed of multiple joints with specific phase shift to maintain some locomotion pattern in the moving process. In this chapter. We will move to the control scheme for the entire undulatory robot system in given situations. Considering in a confined space (Figure 4.1 (a)), there lives a group of undulatory swimmers. Assuming the only interactions between them are passive body contact with individual's neighbors, we were trying to study how effective and robust the group behavior can emerge from this type of simple interaction in close proximity. We simplified each swimmer into a 3-link rigid body robot with two rotational joints (Figure 4.1 (b)). For the robot actuation, we introduced CPG-based collision-driven adaptive phase oscillator as the joint controller to capacitate the robot proprioceptive ability. Robot could understand the local contact events and actively adjust the swimming pattern by phase adaptation according to its neighbors' behavior without any sensory feedback, realizing in-phase or opposite-phase configurations.

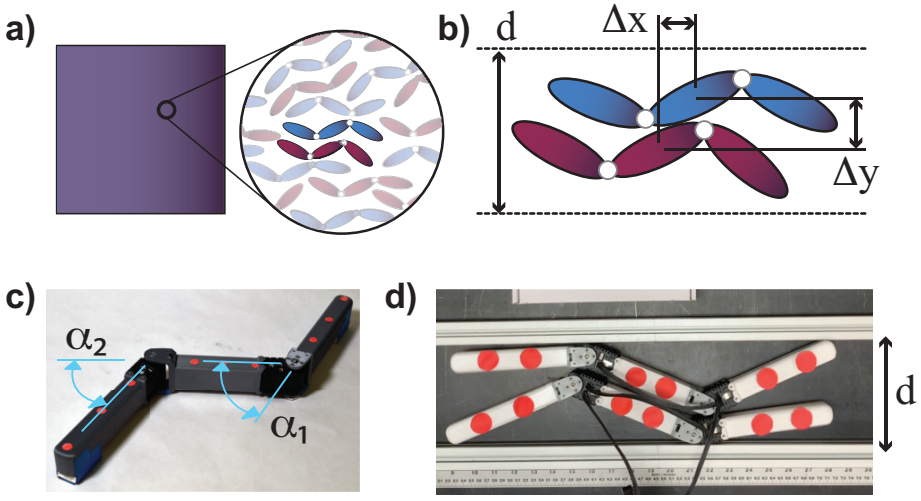

Figure 4.1: Motivation and overview for contact compatibility among undulatory swimmers.

4.1 Control Scheme for Undulatory Locomotion

The bio-inspired n-link robot can accomplish body undulations through oscillatory networks, comprising of $n-1$ actuated joints that oscillate with a positive phase lag between neighbor links from head to tail. A complete travelling wave are expected to generate through a set of position points $\alpha_1, \alpha_2, ..., \alpha_{n-1}$, whose phases $\phi_1, \phi_2, ..., \phi_{n-1}$ uniformly distribute around one cycle, using following equation:

$$\alpha_i = r_i \cos(\phi_i) \qquad i = 1, 2, ..., n-1 \tag{4.1}$$

where r_i and ϕ_i are governed by proposed Collision-driven adaptive phase oscillator:

$$\begin{aligned} \dot{\phi}_i &= \omega + \gamma \times g(\phi_{ei}, \phi_i) \\ \dot{r}_i &= r_i(\mu - r_i^2) \end{aligned} \tag{4.2}$$

The framework enables the phase adaption effect to emerge between different joints through collisions. However, for a single robot agent, the joint-joint relationship is arrayed by the initial conditions of each phase state. The collision sensitive nature can easily break down the

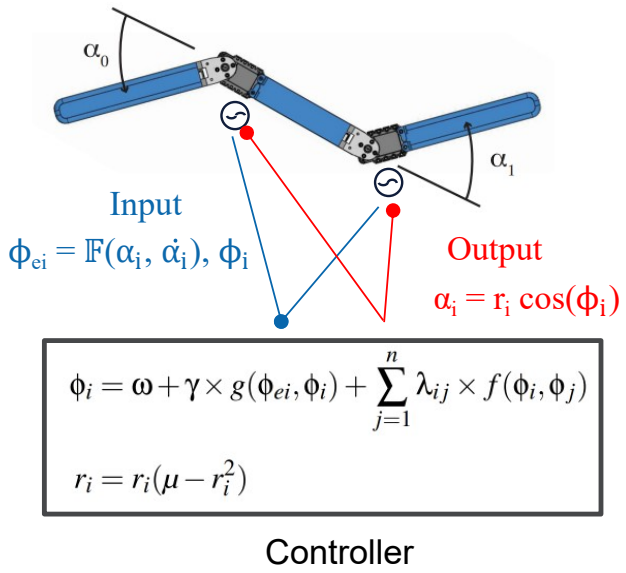

Figure 4.2: Control scheme for multi-link robot.

relationship in the process of robot interaction. It is difficult to retain a stable traveling wave under extreme collision scenario because the phase states are perturbed by the adaption effect frequently. Therefore, we introduce the concept of Central Pattern Generator (CPG) for the purpose of phase regulation between different joints in each single robot (Figure 4.2):

$$\begin{aligned} \phi_i &= \omega + \gamma \times g(\phi_{ei}, \phi_i) + \sum_{j=1}^{n} \lambda_{ij} \times f(\phi_i, \phi_j) \\ r_i &= r_i(\mu - r_i^2) \end{aligned} \tag{4.3}$$

In Equation 4.3, the adaptive function $g(\phi_{ei}, \phi_i)$ with proprioceptive gain $\gamma \in [0, \omega]$ works as phase adaption term to actively adjust individual phase in swarm system. The function $f(\phi_i, \phi_j)$, a.k.a. CPG function, with inter-CPG couplings $\lambda_{ij} \in [0, 1]$ governs the locomotion pattern through

phase regulation effect between joints. The form of the functions can be considered as:

$$\begin{aligned} g(\phi_{ei}, \phi_i) &= \sin(\phi_{ei} - \phi_i) \\ f(\phi_i, \phi_j) &= \sin(\phi_j - \phi_i - \Delta\phi_{ij}) \end{aligned} \tag{4.4}$$

In this case, the positive gain λ_{ij} guarantees phase difference between states ϕ_i and ϕ_j asymptotically converges to $\Delta\phi_{ij}$ no matter how severely the phase adaption effect exerts on the joints.

4.2 Swarm configuration

In contrast to toy model, swarm robot system take account of more motion information rather than phase states. Phase return map fail to comprehensively conclude the collective behavior in the actual system. It is important to characterize the swarm configuration of the robot system with the collection of motion states that reveal moving potential, such as relative lateral separation and kinematic phase difference. In this section, we introduce two different swarm configurations to study how the proposed control law exerts effect on the robot system and results in various collective behaviors.

4.2.1 Dual-robot system

For dual-robot system, lateral separation Δx and kinematic phase difference $\Delta\phi$ precisely describe the dynamic difference in both spatial and phase dimensions. Therefore, define return map $\mathcal{M}$ as

$$\mathcal{M} : (\phi_d^- = \phi_1^- - \phi_2^-, \Delta x^-) \rightarrow (\phi_d^+ = \phi_1^+ - \phi_2^+, \Delta x^+)$$

which reveal the dynamic information in a time scale (Figure 4.3).

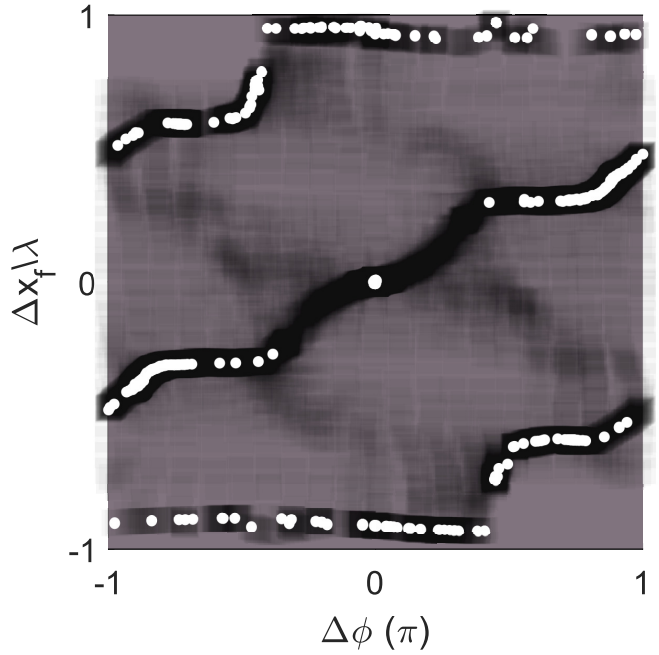

Figure 4.3: Equilibrium lateral separation $\Delta x/\lambda$ (normalized with robot wave length λ) for robot pairs as a function of kinematic phase difference, $\Delta\phi$. White points correspond to equilibrium configurations where robots overlap laterally, gray points are configurations where robots pushed out of contact. The heatmap indicates the effective energy landscape of the equilibrium points.

4.2.2 Multi-robot system

For multi-robot system, the dimensions of $\Delta\phi$ and Δx grows exponentially with the numbers of robots, such that map $\mathcal{M}$ locates in a complicated hyper-plane. Given that we simplified the continuous undulatory locomotion into discrete links oscillation, we define the mean resultant length (MRL) to measure the length of random phase vectors in limit cycle in the following step:

- Obtain robot phase set $[\phi_1, \phi_2, ..., \phi_n]$.
- Calculate

$$C = \sum_{i=1}^{n} \cos\phi_i,\ S = \sum_{i=1}^{n} \sin\phi_i,\ R^2 = C^2 + S^2. \tag{4.5}$$

- Take R as Mean Vector Length (MRL)

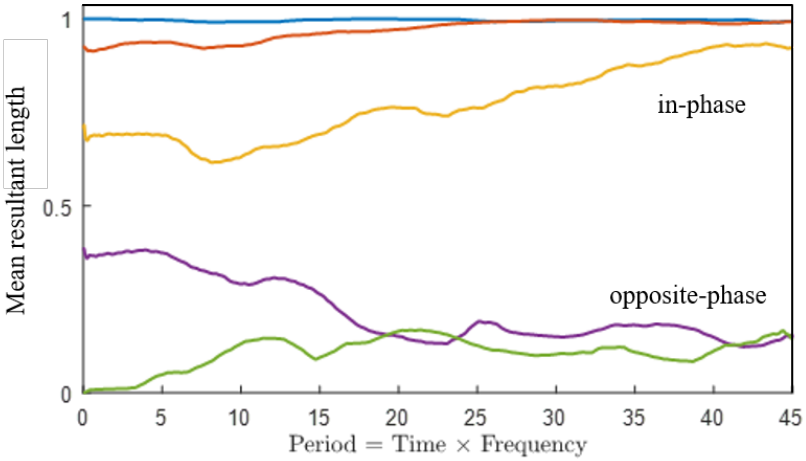

Figure 4.4: Mean resultant length for robot phase as a function of motion period. MRL evolution tendency is determined by initial condition and contact times (reflected by period). In phase synchronization leads to the maximum MRL of 1. Robot group can also reach compatible with a specific value MRL, where phase difference and spatial separation maintain steady.

The configuration emphasizes more on the phase adaption effect between robots. But based on the multiple link simplification, spatial information can be also revealed implicitly (Figure 4.3).

4.3 Experiment and simulation results

In this section, we implement proposed control scheme under different physical environments and observe collective behavior of robot swarms. Swarm configuration is utilized to analyze their moving potential. The control parameters are as Table 4.1 listed.

Table 4.1: Control parameter table

Parameter	Value
μ	40°
ω	π
λ	0.4
$\Delta\phi$	$]\frac{2\pi}{3}, \frac{\pi}{2}[$
γ	[-0.2,1.0]

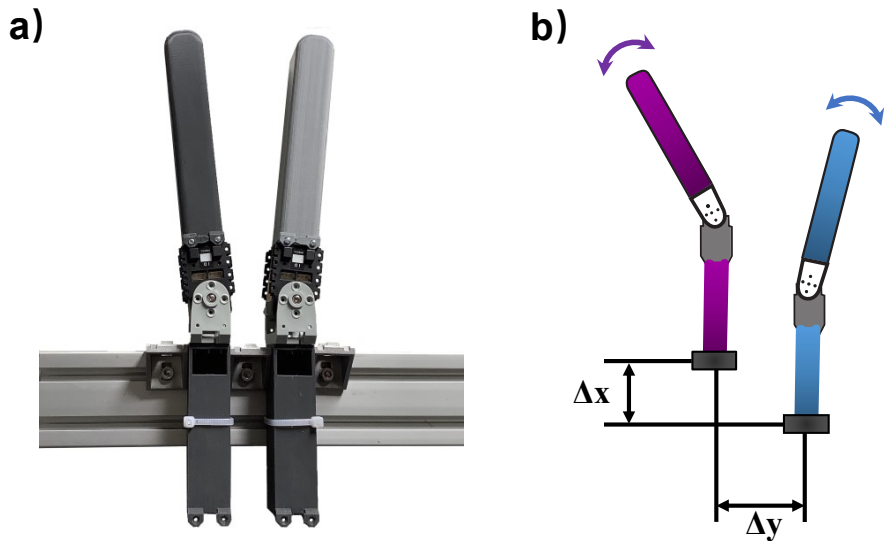

Figure 4.5: Fixed body experiment setup. (a) Two robot bodies were fixed on the guide rail in parallel with an adjustable separation distance. (b) Experiment sketch. Δx and Δy (equivalent to parameter δ in Figure 3.2) represent longitudinal and lateral separation distance respectively.

4.3.1 Two robots are fixed in an adjacent area

Two robots are fixed with specific spatial layouts (Figure 4.5) to imitate some specific scenarios of free motion. We study how proproceptive gain γ and separation distance Δx, Δy

contribute to the shape of phase return map, as a comparison with toy model. Each robot is simplified into two rigid links with one fixed end and one oscillatory joint. The phase difference between the two joints is initialized with $\Delta\phi_0$, ranging from 0 to π with 50 intervals. We measure the change of phase difference within one period (single collision) to generate phase return map under different gain and spatial layouts.

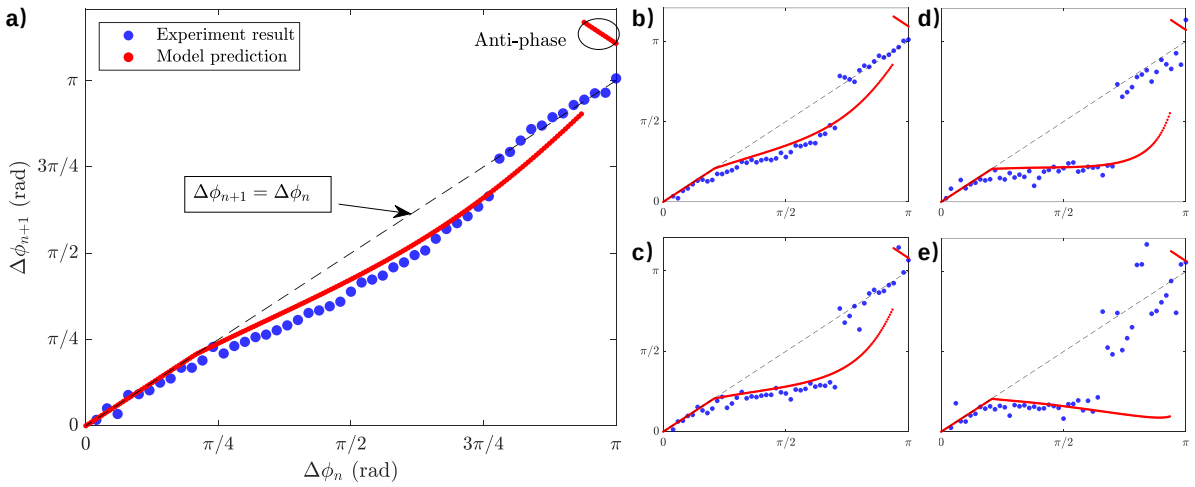

Figure 4.6: The curvature of phase return map depends on proprioceptive gain. Experiments (blue points) with robot pairs were performed to estimate phase return map for varying proprioceptive gain with $\Delta x = 0$, $\Delta y = 0.20$, comparing with model prediction (red points) in section 3. (a)-(e) show experiments with gain = [0.2, 0.4, 0.6, 0.8, 1.0].

Figure 4.6 illustrates that positive gain results in an in-phase synchronization process because the curves are always below $\Delta\phi_{n+1} = \Delta\phi_n$, with a good match of model prediction. Larger gain help increase the curvature of return map, indicating a better adaption effect.

Figure 4.7 and 4.8 partially reproduce some similar scenarios of free motion. When two robots are separated by a specific spatial layouts, they can still get synchronized to some extent. The longitudinal separation Δy do not change the shape of phase return map but always allow behind robot can easily adapt phase to the front because of the unbalanced moment of force.

However, the lateral separation Δx change the phase compatibility, or the effective adaption range. The larger Δx leads to a narrow adaption range ϕ_L.

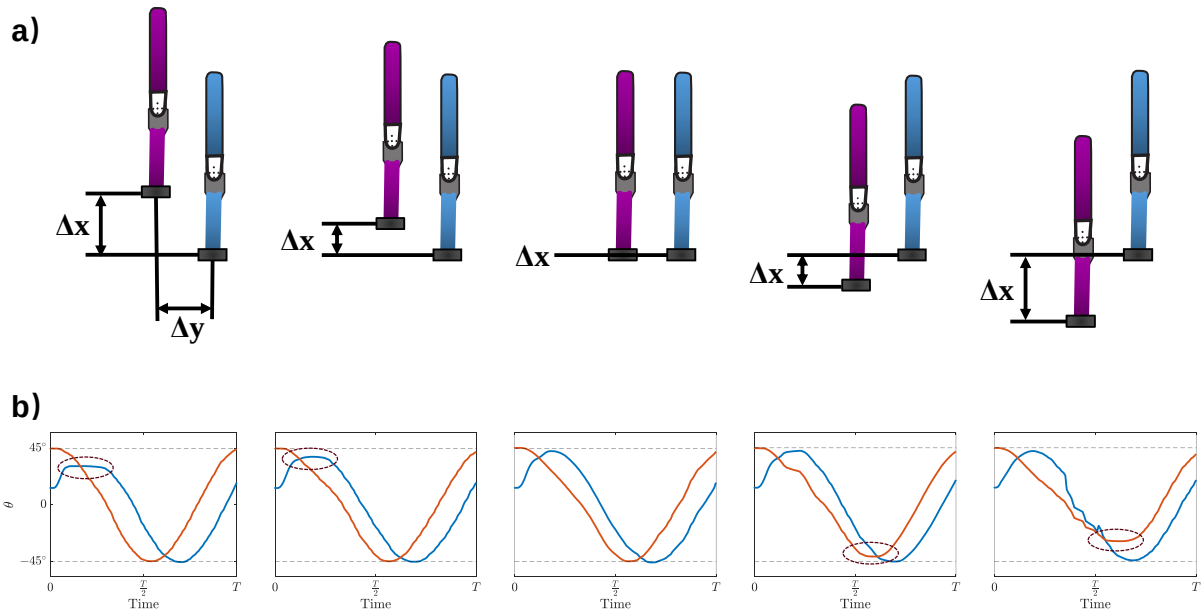

Figure 4.7: The phase adaption process varies with longitudinal separation. (a) Spatial layouts for the robot pairs. $\Delta y = 0.20$ is fixed with varying $\Delta x = [5, 2, 0, -2, -5]$ from left to right. (b) The joint angle adaption process within one period (single collision). The spatially behind robot can easily adapt individual phase to the front one.

Noticeably, the anti-phase region do not appear in any experiments. Because the anti-phase only emerge for large phase difference cases that drive two robots collide extremely with a very large force, the servos may not be able to generate such large force in practice. In other words, the motor triggers some protection mechanism to avoid this happen. Two robots are therefore less likely to reach anti-phase region. If motor can be actuated with force or current directly, e.g. DC motors, the anti-phase phenomena is expected to happen.

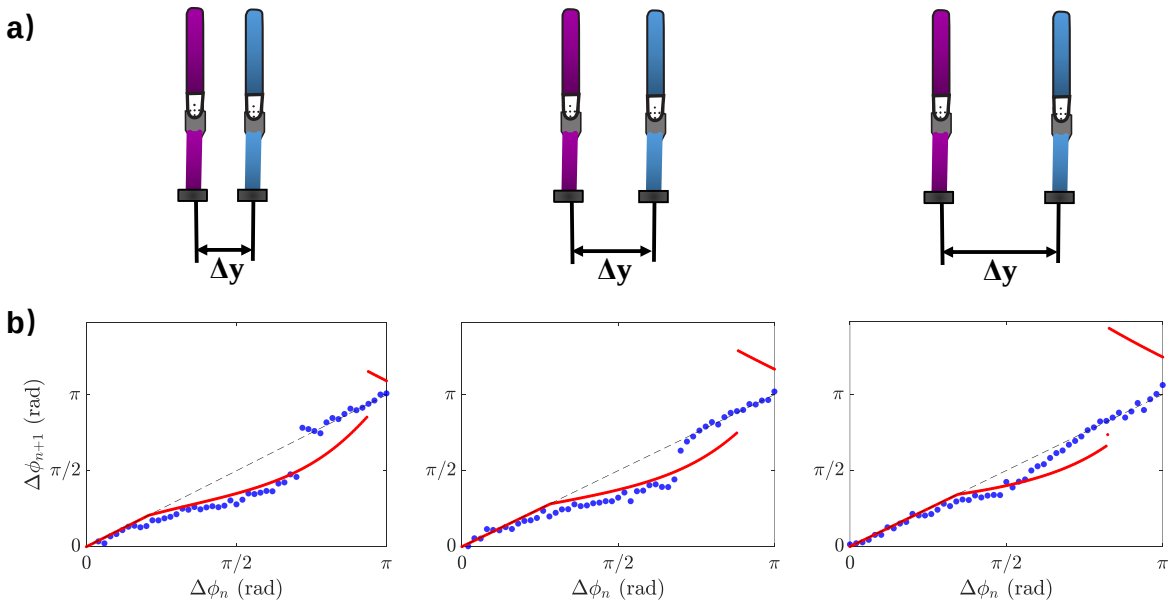

Figure 4.8: The effective adaption region differs from lateral separation. (a) Spatial layouts for the robot pairs. $\Delta x = 0.0$ is fixed with varying $\Delta y = [0.20, 0.36, 0.53]$ from left to right. (b) Phase return map. The compatible region (left bottom) and anti phase region (top right) become larger with the increase of lateral distance.

4.3.2 Robot pair interacts in confined area

Two complete robots are accommodated inside parallel channel for collision interactions (Figure 4.9 (a)). They are initialized with specific phases and centering positions. The channel width CW and proprioceptive gain γ are varying from $0.11m$ to $0.13m$ and 0 to 1 respectively. The relative lateral separation distance Δx and phase difference $\Delta\phi$ are collected to generate swarm configuration. Figure 4.9 (b) shows that three different compatible configurations emerge from synchronization process: one link ahead, in phase and one link behind states. The final states gradually converge to the three compatible regions along the gradient of the heatmap. Figure 4.9 (c) proves that 0 gain is equivalent to open loop and converge to the compatible line. Figure 4.9 (d) and (e) verifies that gain and channel width can help increase the attraction of compatible regions.

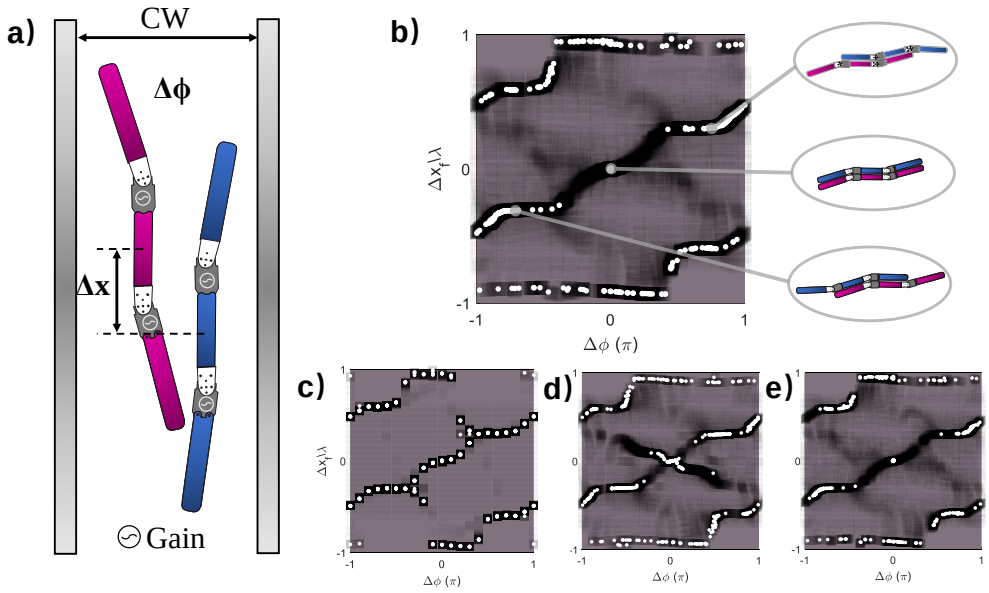

Figure 4.9: The compatible configuration is associated to channel width and proprioceptive gain. (a) Robot pairs may achieve gait compatibility through collision-driven spatial translation and phase adjustment in the confined space. (b) Normalized lateral separation $\Delta x/\lambda$ for robot pairs as a function of kinematic phase difference $\Delta\phi$ (Gain = 0.64, CW = 0.13). White points indicates to compatible states where robots overlap laterally. The heat map reveals the move potential of the system. (c) Gain = 0, CW = 0.13 (d) Gain = 0.64, CW = 0.15 (e) Gain = 0.95, CW = 0.13.

4.3.3 Multiple robots collectively swim in confined space

In contrast to robot pair test, we build four robot system to observe the collective behavior in swarm (Figure 4.10). We conclude that (a) The negative gain (set 1) leads to out of phase synchronization, generating disordered group behavior, (b) The zero gain (set 2) generates compatible motion behavior without phase adaption effect, (c) The positive gain smaller than ω (set 3-4) is able to produce collective in-phase behavior robustly. The larger the gain is, the better synchronization emerge, and (d) The positive gain larger than ω fail the motors for the oscillated frequency.

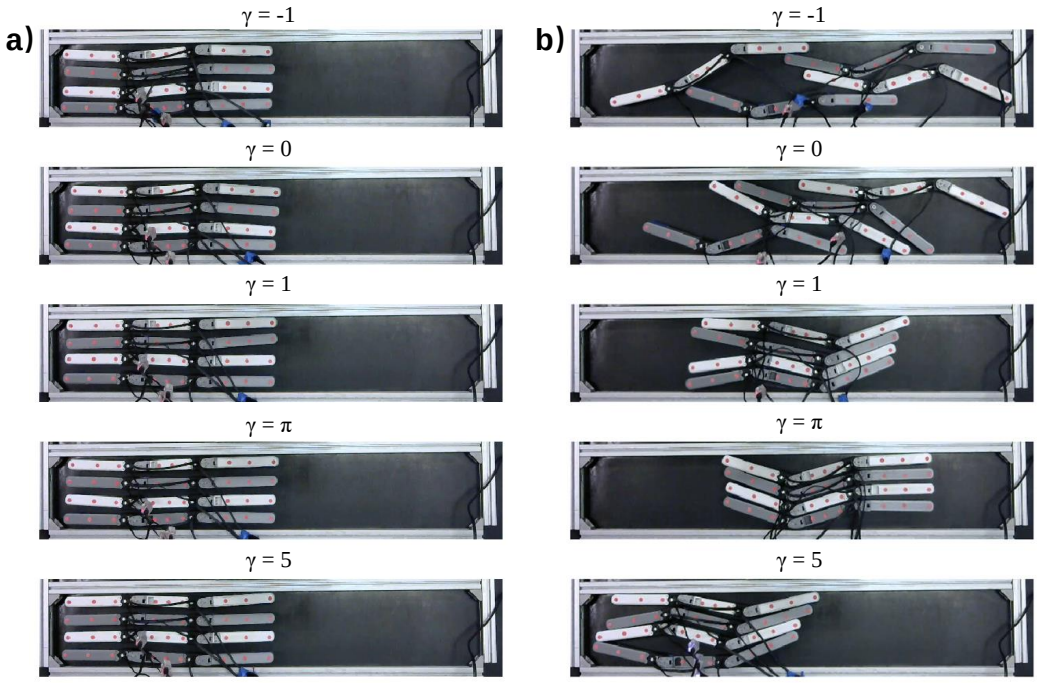

Figure 4.10: Collective behaviors hinges upon adaptive coefficient $\gamma = Gain \times \omega$. (a) Robot groups are actuated with the same intrinsic frequency $\omega = \pi$ but different adaptive coefficient $\gamma = [-1, 0, 1, \pi, 5]$ from top to bottom. (b) The steady motion pattern (from top to bottom): disordered motion, compatible motion, partial synchronized motion, complete synchronized motion and suppressed motion.

4.3.4 Robot pairs passability

We test the robot passiability for the narrow channel by adjusting gain value and channel width. As Figure 4.11 and 4.12, during the first motion stage (around first 10 seconds), the robot locate in a relative free space, the adaption effect have not significantly exerted on robot pairs. Only when traversing the narrow channel, two robots start to interact as a result of positive or negative gain. . The experiments illustrate adaption effect was influenced by two factors: (a) channel width (indicating the collision possibility), and (b) proprioceptive gain. Initially, robot pair do not have an obvious phase adaptation process because weak collision condition. However, when the collision become extreme, phase adaptation effect become remarkable as well. Besides, the synchronized gait also increases their moving efficiency. When we switch the gain to negative, the collective behavior disappear (Figure 4.11 (b)).

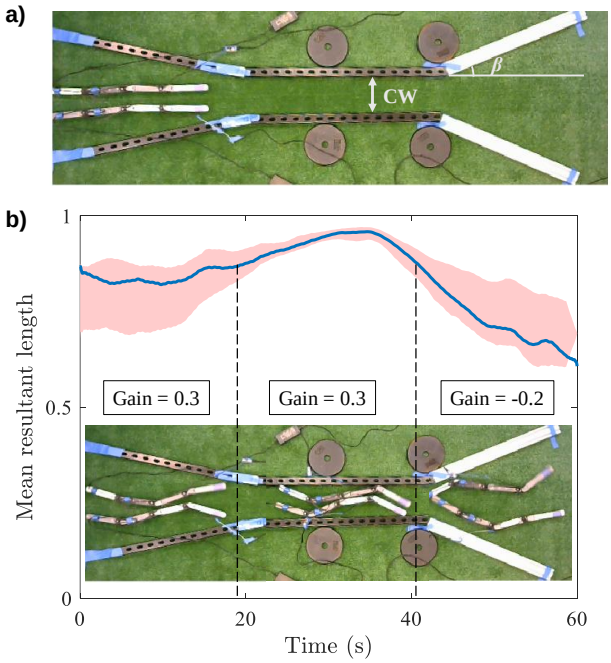

Figure 4.11: Robots pairs is able to traverse the narrow channel with positive proprioceptive gain and maintain locomotion pattern after separation.

4.3.5 Energy and efficiency

Lastly, we figure out why animals prefer to the collective motion. The simulation (Figure 4.13) is carried out to test two different swimming gaits. The top group is asynchrony group with proprioceptive gain of 0. The below group is synchrony group with positive gain. We found that the synchrony group swims much faster than asynchrony. Besides, the synchrony group consumes less energy than asynchrony (Figure 4.14).

4.4 Summary

The chapter presents the control scheme works effectively in robot swarm system for phase adaption purpose. With help of swarm configurations, we develop a qualitative and quantitative understanding of synchronization process. Synchronized gait help robot swarm traverse narrow channel. We also look the process into energy and efficiency aspects, which

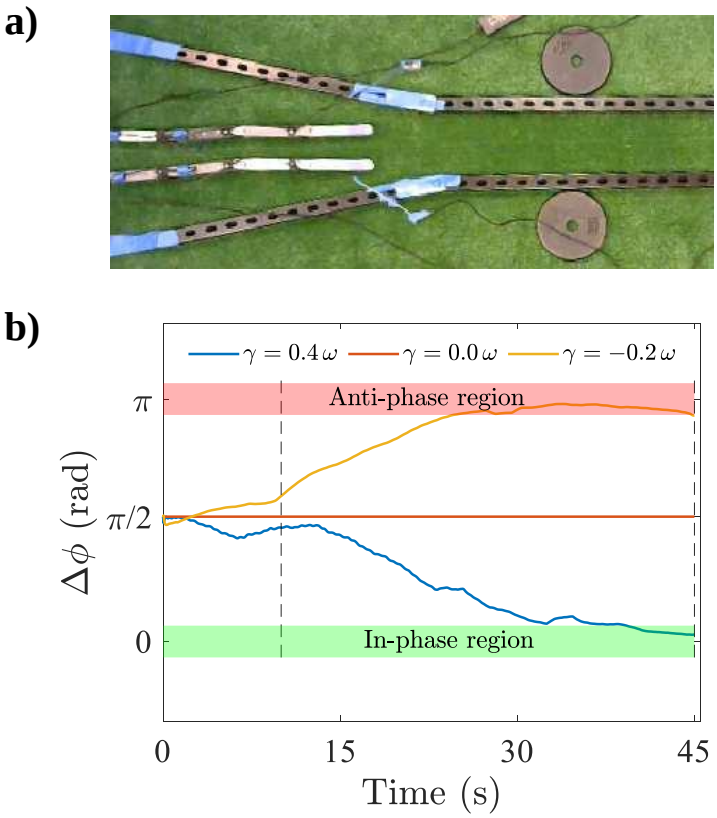

Figure 4.12: Passability test. (a) An overhead picture of two robots challenged to move through a narrow channel. (b) Relative phases between the two robot showing: in-phase synchronization at $0 < \gamma < \omega$, anti-phase synchronization at $\gamma < 0$, and non-feedback at $\gamma = 0$.

might be the biological nature of collective swimming.

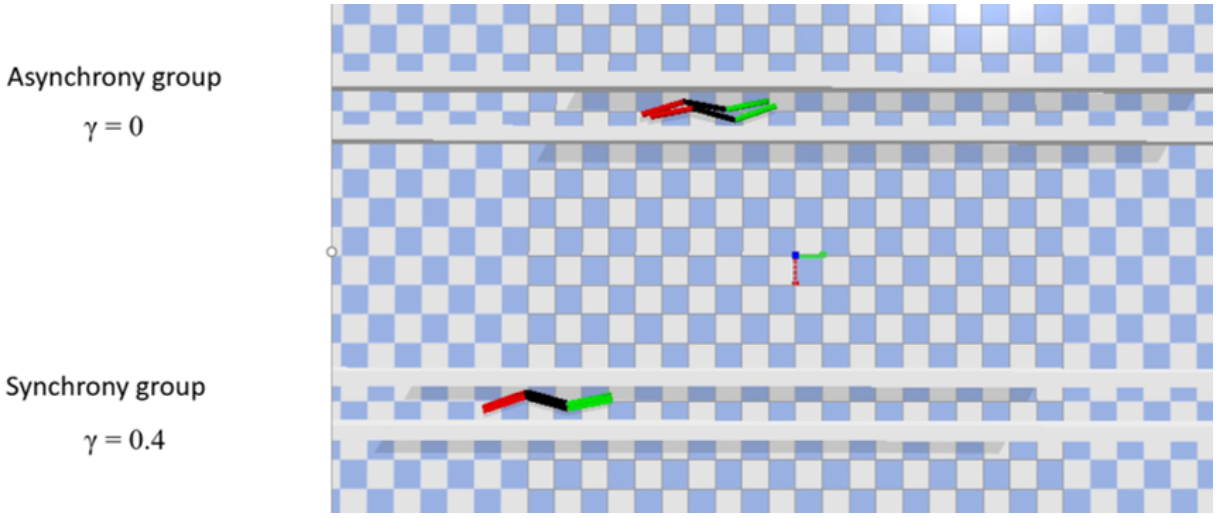

Figure 4.13: Simulation: two robots traverse 15 *m* with synchronous gait and asynchronous gait

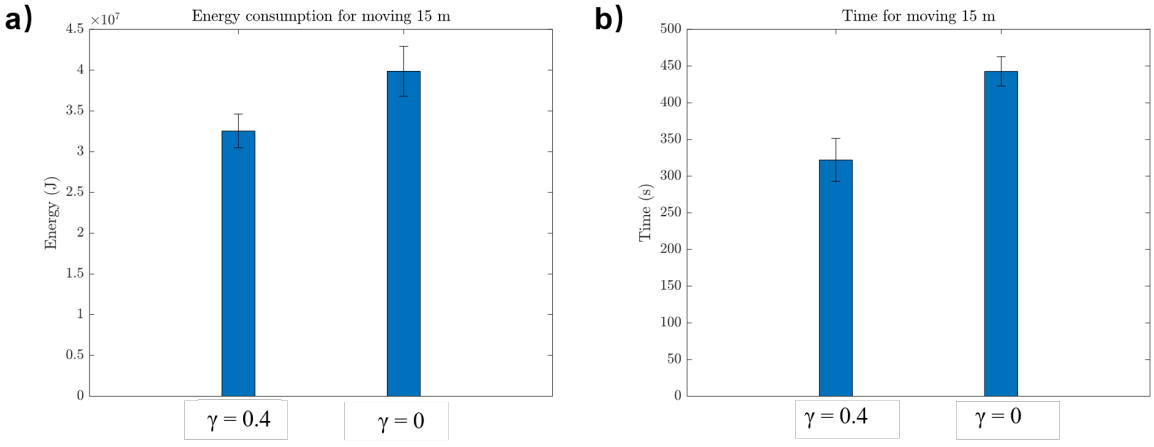

Figure 4.14: Energy consumption (left) and moving efficiency

Chapter 5

Conclusions

In this study, we demonstrate that undulatory motion in biologically inspired robots can be synchronized through contact interactions without the need for robot-robot communication. The shape of phase return map hinge on proprioceptive gain and adaptive function. Proprioceptive feedback inspired from neuromechanical studies of *C. elegans* enable emergent synchronization and determine the pattern of collective behaviors. Robot pairs that traverse narrow channels are able to synchronize their gait to move effectively together in confined space. Synchronized behavior help on both energy consumption and motion efficiency. Overall these results suggest new methods for designing feedback control of emergent synchronization in robot swarm.

Bibliography

[1] Shay Gueron, Konstantin Levit-Gurevich, Nadav Liron, and Jacob J Blum. Cilia internal mechanism and metachronal coordination as the result of hydrodynamical coupling. *Proceedings of the National Academy of Sciences*, 94(12):6001–6006, 1997.

[2] Christopher Wollin and Holger Stark. Metachronal waves in a chain of rowers with hydrodynamic interactions. *The European Physical Journal E*, 34(4):1–10, 2011.

[3] Brian Button, Li-Heng Cai, Camille Ehre, Mehmet Kesimer, David B Hill, John K Sheehan, Richard C Boucher, and Michael Rubinstein. A periciliary brush promotes the lung health by separating the mucus layer from airway epithelia. *Science*, 337(6097):937–941, 2012.

[4] A Gopinath and L Mahadevan. Elastohydrodynamics of wet bristles, carpets and brushes. *Proceedings of the Royal Society A: Mathematical, Physical and Engineering Sciences*, 467(2130):1665–1685, 2011.

[5] Jens Elgeti and Gerhard Gompper. Emergence of metachronal waves in cilia arrays. *Proc. Natl. Acad. Sci. U. S. A.*, 110(12):4470–4475, March 2013.

[6] Gwynn J Elfring and Eric Lauga. Hydrodynamic phase locking of swimming microorganisms. *Phys. Rev. Lett.*, 103(8):088101, August 2009.

[7] Jinzhou Yuan, David M Raizen, and Haim H Bau. Gait synchronization in caenorhabditis elegans. *Proc. Natl. Acad. Sci. U. S. A.*, 111(19):6865–6870, May 2014.

[8] Raghunath Chelakkot, Michael F Hagan, and Arvind Gopinath. Synchronized oscillations, traveling waves, and jammed clusters induced by steric interactions in active filament arrays. *Soft Matter*, December 2020.

[9] Christopher Fang-Yen, Matthieu Wyart, Julie Xie, Risa Kawai, Tom Kodger, Sway Chen, Quan Wen, and Aravinthan DT Samuel. Biomechanical analysis of gait adaptation in the nematode caenorhabditis elegans. *Proceedings of the National Academy of Sciences*, 107(47):20323–20328, 2010.

[10] Quan Wen, Michelle D Po, Elizabeth Hulme, Sway Chen, Xinyu Liu, Sen Wai Kwok, Marc Gershow, Andrew M Leifer, Victoria Butler, Christopher Fang-Yen, Taizo Kawano,

William R Schafer, George Whitesides, Matthieu Wyart, Dmitri B Chklovskii, Mei Zhen, and Aravinthan D T Samuel. Proprioceptive coupling within motor neurons drives c. elegans forward locomotion. *Neuron*, 76(4):750–761, November 2012.

[11] Michael Sfakiotakis and Dimitris P Tsakiris. Neuromuscular control of reactive behaviors for undulatory robots. *Neurocomputing*, 70(10-12):1907–1913, 2007.

[12] Örjan Ekeberg. A combined neuronal and mechanical model of fish swimming. *Biological cybernetics*, 69(5):363–374, 1993.

[13] Auke Jan Ijspeert. A connectionist central pattern generator for the aquatic and terrestrial gaits of a simulated salamander. *Biological cybernetics*, 84(5):331–348, 2001.

[14] Richard H Rand, Avis H Cohen, and Philip J Holmes. Systems of coupled oscillators as models of central pattern generators. *Neural control of rhythmic movements in vertebrates*, pages 333–367, 1988.

[15] Wei Zhou, Jaquelin Dezha-Peralta, Zhuonan Hao, and Nick Gravish. Synchronized swimming: collisions drive gait compatibility in undulatory robots, 2020.

[16] SH Strogatz. Nonlinear dynamics and chaos: with applications to physics, biology, chemistry, and engineering, 1st pbk, 2000.

[17] Wei Zhou, Zhuonan Hao, and Nick Gravish. Collective synchronization of undulatory movement through contact. *arXiv preprint arXiv:2012.07124*, 2020.

[18] Aksel Andreas Transeth. Modelling and control of snake robots. 2008.

[19] Jonas Buchli, Ludovic Righetti, and Auke Jan Ijspeert. Engineering entrainment and adaptation in limit cycle systems. *Biological Cybernetics*, 95(6):645–664, 2006.

[20] Ludovic Righetti, Jonas Buchli, and Auke Jan Ijspeert. Dynamic hebbian learning in adaptive frequency oscillators. *Physica D: Nonlinear Phenomena*, 216(2):269–281, 2006.

[21] Ludovic Righetti, Jonas Buchli, and Auke Jan Ijspeert. Adaptive frequency oscillators and applications. *The Open Cybernetics & Systemics Journal*, 3(1), 2009.

[22] Yoshiki Kuramoto. *Chemical oscillations, waves, and turbulence*. Courier Corporation, 2003.

[23] Jonas Buchli, Fumiya Iida, and Auke Jan Ijspeert. Finding resonance: Adaptive frequency oscillators for dynamic legged locomotion. In *2006 IEEE/RSJ International Conference on Intelligent Robots and Systems*, pages 3903–3909. IEEE, 2006.

[24] Auke Jan Ijspeert. Central pattern generators for locomotion control in animals and robots: a review. *Neural networks*, 21(4):642–653, 2008.

[25] James J Collins and Sally A Richmond. Hard-wired central pattern generators for quadrupedal locomotion. *Biological cybernetics*, 71(5):375–385, 1994.

[26] Auke Jan Ijspeert and Alessandro Crespi. Online trajectory generation in an amphibious snake robot using a lamprey-like central pattern generator model. In *Proceedings 2007 IEEE International Conference on Robotics and Automation*, pages 262–268. IEEE, 2007.